Watching Plasmon-Induced Nanoparticle Ostwald Ripening

Francis M. Alcorn[a, b], Maya Chattoraj[a], Renske M. van der Veen, [a, b, c] and Prashant K. Jain[a, b,*]

[a] Department of Chemistry, University of Illinois Urbana–Champaign, Urbana, Illinois 61801, United States

[b] Materials Research Laboratory, University of Illinois Urbana–Champaign, Urbana, Illinois 61801, United States

[c] Helmholtz Zentrum Berlin für Materialien und Energie GmbH, 14109 Berlin, Germany

E-mail: jain@illinois.edu

Abstract:

Light-absorbing plasmonic nanostructures are being used in a variety of applications, including photocatalysis and sensing. Because structure is intricately linked to function and performance, it is essential to understand how the structures of these materials might evolve under light excitation and what are the types and atomic natures of these structural transformations. Using a transmission electron microscope equipped with the capability of laser excitation of the specimen, we monitored the structures of Au–Cu alloy nanoparticles under plasmonic excitation. Plasmonic excitation was found to induce Ostwald ripening of nanoparticles. This process occurs in a switch-like manner distinct from electron-beam-induced coalescence that we also observe. This structural transformation is not induced by heating and is an example of a nonthermal structural transformation induced by plasmonically excited carriers. These results inform us about potential transformations of plasmonic nanostructures that can occur under operating conditions of plasmonic photocatalysis or plasmon-assisted electrocatalysis where a high areal density of plasmonic nanoparticles supported on a substrate is subjected to continuous light excitation.

Introduction

Plasmonic nanostructures are characterized by their strong interaction with light, which arises from collective charge carrier oscillations known as a localized surface plasmon resonance (LSPR).[1,2] Plasmonic properties and resulting applications of these materials in solar energy harvesting catalysis,[3–6] sensing,[7–9] biomedicine,[7,10,11] and optoelectronics devices,[12–14] are innately linked to the structures of these materials. This is particularly true for catalytic properties, which are often determined by size, shape, surface faceting, and surface composition of the nanostructure.[15–21] However, nanostructures are unlikely to be invariant under reactive environments and energetic stimuli used in catalytic processes. Their structures can evolve, which in turn can promote or mar catalytic activity.

The structural evolution of nanomaterials under perturbative conditions has been studied by optical spectroscopy,[22–26] X-ray techniques,[27–29] and in situ transmission electron microscopy (TEM).[30–36] In particular, TEM enables studies of such dynamics at the single-nanoparticle level with atomic spatial resolution and millisecond temporal resolution[36–38] or faster using a pump–probe method.[36,39,40] However, TEM has rarely been used to probe structural transformations induced by light excitation.[41] The few in-situ TEM studies of nanomaterials under light have uncovered unexpected photocatalytic pathways[42,43] and photocatalyst activation dynamics,[44] among a host of interesting fast and ultrafast dynamics.[36,40,45–53] However, real-time TEM imaging of the plasmon-induced structural evolution of plasmonic nanostructures remains an unmet opportunity.

Herein, we describe an in situ TEM study of plasmonic Au–Cu alloy nanoparticles, a material of interest for light-to-chemical energy conversion applications including plasmon-assisted CO_2 reduction,[54,55] under light irradiation.[53] We observe plasmon-induced transformations of these nanoparticles akin to Ostwald ripening. The process is switch-like involving a rapid reshaping to spherical morphologies following a relatively long waiting time for initiation. Unlike the ripening process induced by plasmonic excitation, electron-beam effects induce coalescence into irregular anisotropic nanostructures. We also observe few-atom-wide interparticle neck formation and grain boundary formation in these processes. These results inform on potential transformations that can occur in substrate-supported plasmonic nanostructures used for plasmonic catalysis and electrocatalysis.

Methods:

Au–Cu alloy nanoparticles were chosen on account of their plasmonic and catalytic properties, which are expected to be leveraged in plasmon-assisted catalytic processes.[54,55] Au–Cu alloy nanoparticles were synthesized by a seed-based method, as further detailed in the SI. First, Au seed nanoparticles were synthesized using a method described by Peng et al.[56] Briefly, a Au precursor salt, $HAuCl_4$, was reduced by tert-butylamine borane in oleylamine and tetralin. These Au nanoparticles were then alloyed with Cu using a method described by Chen et. al..[57] A dispersion of the Au nanoparticles in hexane was mixed with a Cu precursor salt, $Cu(CH_3COO)_2$, in oleic acid and tri-n-octylamine. The synthesized Au–Cu alloy nanoparticles were then isolated by centrifugation and redispersed in hexane. Characterization by TEM, X-ray diffraction (XRD), and ultraviolet–visible (UV–vis) extinction spectrophotometry was performed, as further detailed in the SI. Nanoparticles had an average diameter of 2.3 nm with a standard deviation of 0.9 nm (Figure S1). XRD analysis suggests a face-centered-cubic (FCC) lattice and an alloy of ~70% Au and ~30% Cu (Figure S1). UV–vis extinction spectroscopy shows an LSPR band centered around 550 nm (Figure S1).

TEM experiments were performed using a Hitachi H-9500 dynamic environmental transmission electron microscope (DETEM)[53] operated at an accelerating voltage of 300 kV. A 1–2 μL dispersion of Au–Cu nanoparticles in hexane was dropcast on an ultrathin carbon film on lacey carbon supported on a 400-mesh Cu TEM grid (Ted Pella). The sample was then cleaned using a Tergeo EM plasma cleaner with an $Ar+O_2$ plasma for 2 min at 10 mW power, a 64/255 duty cycle, and a "remote mode" setting. For probing structural transformations under plasmon-excitation conditions, the sample was irradiated with a Bright Solutions 532 nm laser (<1 ns pulse width, 80 kHz repetition rate, ~700 μm^2 spot area) introduced into the sample chamber of the DETEM. In one subset of experiments under plasmonic excitation, a group of nanoparticles was imaged before and after several minutes of irradiation by the laser at 4–5 mW power, i.e., 7–9 mJ/cm^2 per pulse fluence. In the interim period, the electron beam was blanked by turning off the gun valve. In another subset of experiments under plasmonic excitation, in-situ imaging was performed with a widely spread electron beam, maintaining a relatively low electron dose rate (< 400 electrons/$Å^2$/s) while irradiating with the laser at ~4–5 mW. To counteract the reduced signal-to-noise that results from the lower electron dose rate and sample vibrations induced by laser

irradiation, the electron beam was defocused to improve imaging contrast. For in-situ experiments without plasmonic excitation, imaging was performed with a more condensed electron beam maintaining higher electron dose rates on the order of 1000–2000 electrons/Å^2/s.

TEM images and in-situ movies were acquired with an UltraScan 1000 electron detector except for several atomic-resolution movies of electron-beam-induced coalescence (Figs. 4 and 5b–d), which were acquired using a Gatan K2 direct electron detector. Pre- and post- mortem images were saved as DM4 format files, and in-situ movies were saved as AVI files. Videos were binned (2 × 2) to keep file sizes manageable. Processing and analysis of data were performed in ImageJ and OriginPro, as further detailed in the SI.

Results and Discussion:

Several plasmon-induced structural transformations are identified by comparing TEM images before and after 5 min of plasmonic excitation (5 mW, ~9 mJ/cm^2 per pulse) of a group of nanoparticles with electron-beam irradiation turned off during the 5 min period (Figures 1a, b and S2). Several nanoparticles, encircled in red in Figure 1a, increased in size, as determined from their projected areas (see SI section for details of data analysis). Additionally, several nanoparticles disappeared, indicated by the light blue circles in the post-mortem image after irradiation (Figure 1b). The growth of some nanoparticles with concomitant disappearance of adjacent nanoparticles suggests that plasmonic excitation induces an Ostwald ripening-like process of nanoparticles.[58,59] In Ostwald ripening, smaller particles dispersed in a liquid or solid medium undergo dissolution, while the solute generated by dissolution gets concurrently deposited on larger nanoparticles.[60,61] Although there is no solvent in our experiments, which are performed under vacuum conditions, the substrate surface may be involved in mediating mass transfer between the nanoparticles. While ablation or evaporation may instead be responsible, these processes are expected to be manifested in an overall loss of volume from the nanoparticles. A systematic loss of volume is not observed in our analysis (Table S1). There are some nonextreme cases of coalescence: for instance, the nanoparticle encircled by the yellow dotted line in Figure 1 did not fully disappear but decreased in size (see SI) while neighboring nanoparticles grew.

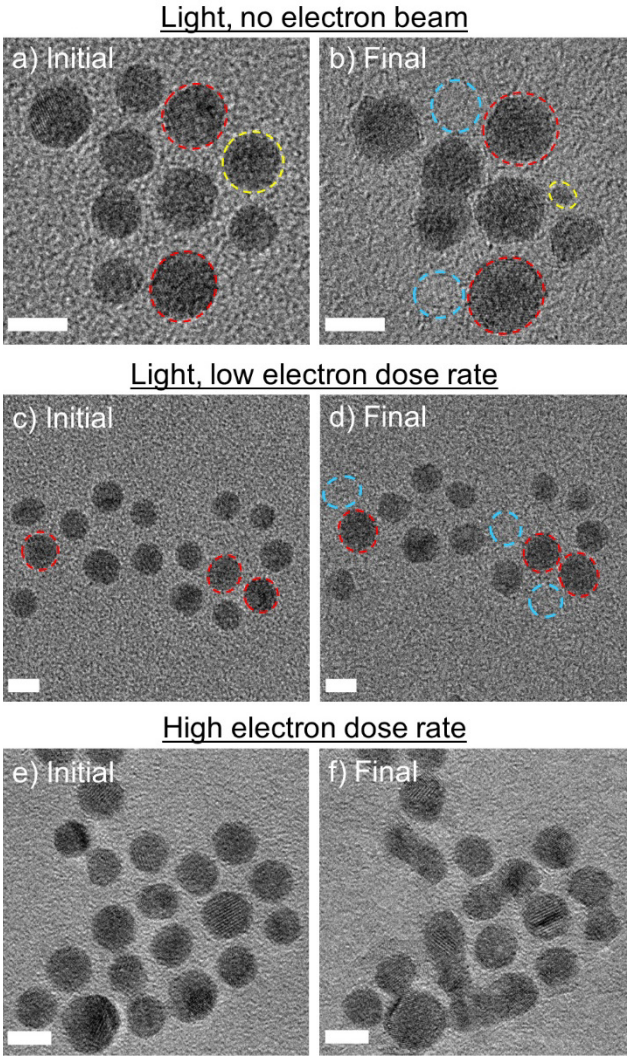

Figure 1. TEM imaging of plasmon-induced Ostwald ripening and electron-beam-induced coalescence. TEM image acquired (a) before and (b) after laser irradiation (5 mW or ~9 mJ/cm^2 per pulse for 5 min) of a group of nanoparticles while the electron beam was kept off during laser irradiation. Several nanoparticles (encircled by dotted red line), increased in size as determined from their projected areas; while nearby nanoparticles (encircled by dotted blue line) disappeared. One nanoparticle (encircled by a dotted yellow line) decreased in size while neighboring nanoparticles grew. TEM image acquired (c) before and (d) after laser irradiation (5 mW or ~9 mJ/cm^2 per pulse for 10 min) of a group of nanoparticles at a low electron dose rate of the order of 200–300 electrons/Å^2/s. In this case as well, some nanoparticles (encircled by red dotted lines) grow, and nanoparticles (encircled by blue dotted lines) disappear. TEM image acquired (e) before and (f) after a period of 11 min electron-beam exposure at higher electron dose rates of the order of 1000 electrons/Å^2/s without laser irradiation. In this case, irregular morphologies appeared to form by coalescence; however, no nanoparticles disappeared. All scale bars are 5 nm in length.

To investigate this further, we conducted in situ TEM to follow the structural transformations of the nanoparticles in real time. Similar structural transformations were observed for groups of nanoparticles imaged in real time under plasmonic excitation with low electron dose rates (Figure 1c,d and Supporting Movie). Specifically, nanoparticle disappearance was seen under plasmonic excitation both without electron-beam irradiation (Figure 1a,b) and with electron-beam

irradiation (Figure 1c,d), which confirms that the process is induced by plasmon excitation. Conversely, in the absence of plasmonic excitation, continuous electron-beam exposure at higher electron-beam dose rates (~1000 electrons/Å^2/s) induced the fusing or coalescence of closely spaced nanoparticles into irregular, anisotropic nanostructures with no nanoparticle disappearance evident (Figure 1e,f).

Plasmon-induced Ostwald ripening exhibits interesting kinetics as seen from movies (snapshots from one example presented in Figure 2) and time trajectories (Figure 3). Typically, there is a long waiting or initiation period following which there is rapid, almost switch-like absorption of one nanoparticle by another.[22,62] In one such instance, a nanoparticle (encircled by the dotted red line in Figure 2a) persisted for 224 s of plasmonic excitation but it then disappeared, i.e., it was fully absorbed by the neighboring nanoparticle, by 226 s. In other words, Ostwald ripening required <2 s, two orders of magnitude shorter than the waiting time of ~225 s. In contrast, electron-beam-induced coalescence did not proceed in a switch-like manner but rather involved gradual reshaping of a pair of nanoparticles into an irregularly shaped, anisotropic nanostructure (snapshots from an example movie presented in Figure 2b).

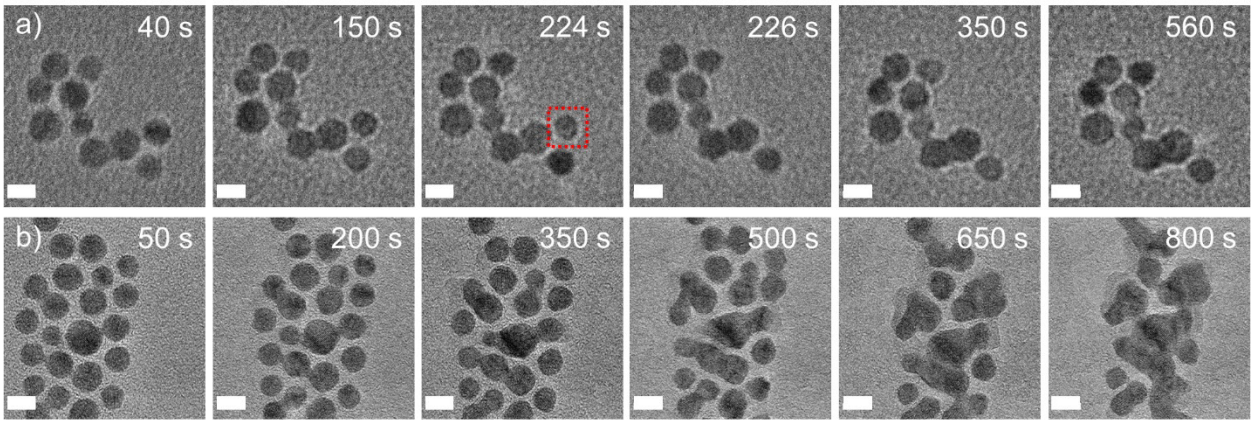

Figure 2. Switch-like nature of plasmon-induced Ostwald ripening contrasted with gradual electron-beam-induced coalescence. (a) Snapshots from a movie of a group of nanoparticles imaged under plasmonic excitation (4 mW, ~7 mJ/cm^2 per pulse) at a low electron dose rate of the order of 100 electrons/Å^2/s. One nanoparticle (indicated by the red box) persisted for 224 s under plasmonic excitation but it fully disappeared between 224 s and 226 s. Each snapshot is labeled by the time duration under plasmonic excitation. (b) Snapshots from a movie of a group of nanoparticles imaged under high-dose-rate electron-beam exposure of the order of 2000 electrons/Å^2/s and no plasmonic excitation showing nanoparticle coalescence by a gradual reshaping process. Each snapshot is labeled by the time duration under electron-beam exposure. Scale bars are 5 nm in length.

The switch-like kinetics of plasmon-induced Ostwald ripening is quantitatively characterized by analyzing trajectories of projected nanoparticle areas as a function of time under

laser irradiation (Figure 3) produced from in-situ movies, as described in the SI. Each trajectory was fit to a sigmoidal function of the form:

$$I(t) = \frac{I_1 - I_2}{1 + e^{\frac{t-t_0}{dt}}} + I_2 \qquad (1)$$

where I denotes the integrated counts of a frame at time t, t_0 is the waiting time, and dt represents a time constant for the rapid ripening event. I_1 and I_2 are fit parameters that reflect the asymptomatic values of the counts respectively at early and late times in a trajectory. We examined the statistics of the kinetic parameters, t_0 and dt across seven trajectories of Ostwald ripening events. Waiting times were at least 1 order of magnitude longer than the ripening time constants, with mean ± standard deviation of 180 ± 120 s for the former and 5 ± 4 s for the latter. This quantitatively confirms the switch-like nature of the ripening process.

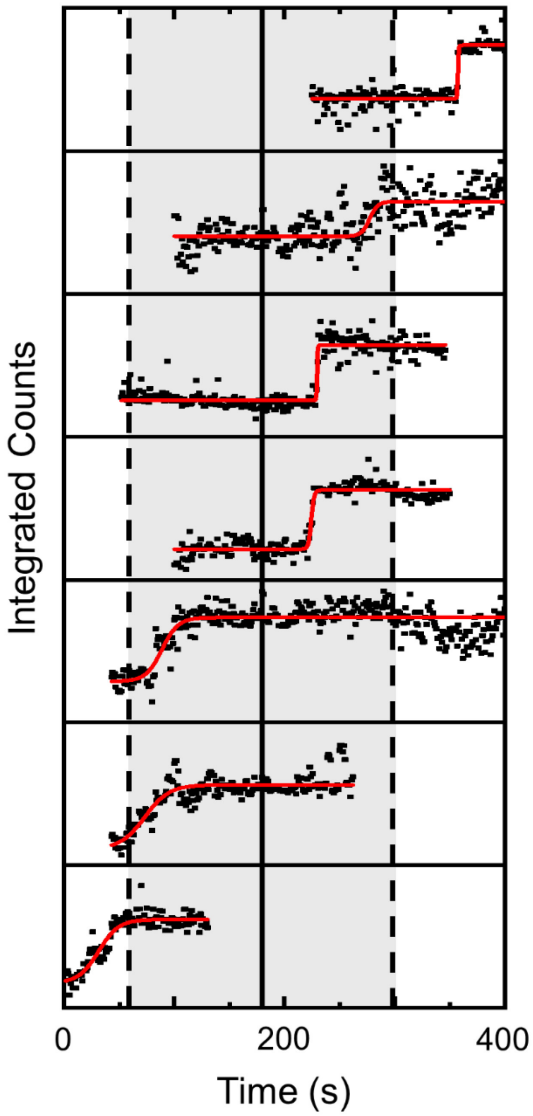

Figure 3. Plasmon-induced Ostwald ripening kinetics. Seven time trajectories (black points) of the Ostwald ripening process under plasmonic excitation. Each trajectory is a plot of the integrated counts as a function of the time duration under plasmonic excitation and is fit (red line) to eq 1. Vertical line marks the mean waiting time across all seven trajectories and the shaded area denotes the mean ± standard deviation of the waiting time.

Next, we examined the role of plasmonic excitations. Plasmon excitation is known to decay on the 1 ps time scale by the generation of excited carriers with eventual dissipation of energy by electron–phonon cooling which leads to photothermal heating of the nanoparticle surface. We examined whether the temperature elevation caused by such photothermal heating could be responsible for inducing Ostwald ripening. Heating the nanoparticles to temperatures up to 500 ºC in the absence of plasmon excitation did not induce any Ostwald ripening (Figure S3). This alludes to a nonthermal effect involving excited carriers generated by plasmonic exciation. Hot carriers generated by photoexcitation of Au nanoparticles undergo ultrafast relaxation by electron–phonon

scattering. Particularly, in small nanoparticles of the size studied here, the relaxation can occur primarily through the excitation of surface phonon modes,[63] which can mobilize surface atoms[64] and even induce nonthermal melting at the surface,[65] dynamics that could be directly imaged with sufficient advances in ultrafast electron microscopy.[36,51,66] This surface mobilization of atoms may be the initiator of ripening or coalescence, as we observed by atomic-resolution imaging. In the course of electron-beam-induced coalescence, a few-atom-wide neck forms on the surface of a nanoparticle and extends to the surface of a neighboring nanoparticle (Figure 4). Although such atomic-resolution imaging was not possible under plasmonic excitation conditions due to laser-induced vibrations, we reason that the findings may apply to the plasmon-induced process because the final morphology for nanoparticle pairs undergoing coalescence is similarly spherical for electron-beam-induced and plasmon-induced pathways (Figure S4). However, as described earlier, the kinetics of the plasmon-induced process are markedly different from those of electron-beam induced coalescence: the switch-like nature of the former may be attributed to the low probability of electron–surface phonon scattering due to the preponderance of hot electron–bulk phonon scattering,[63] which renders the initiation of ripening stochastic.

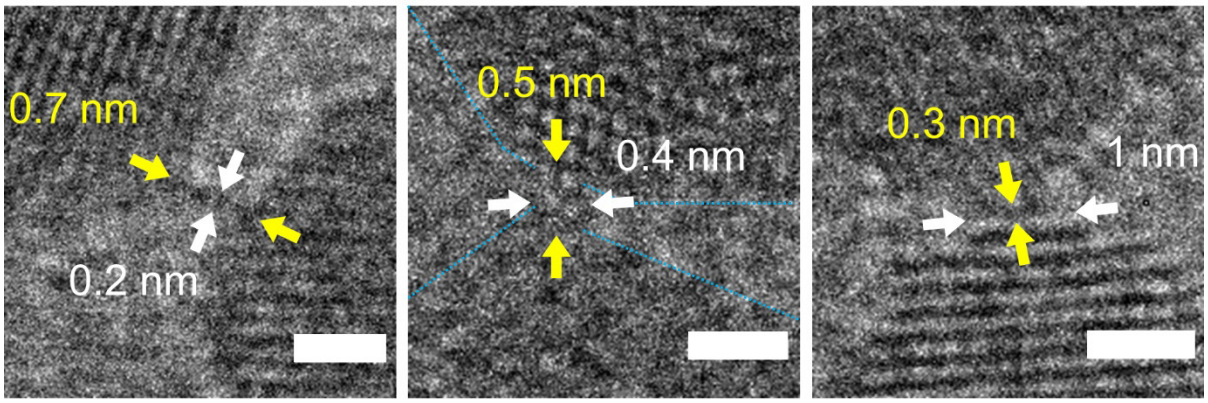

Figure 4. Neck formation between nanoparticles during coalescence. Selected high-magnification TEM images showing few-atom-wide necks formed between nanoparticles. Scale bars are 1 nm in length. The length and width of each neck are labeled in yellow and red font, respectively. From measurements of 39 such instances, the neck width ranged from ~0.2 nm to >2 nm with an average value of 1.14 nm and a standard error of 0.08 nm; neck lengths ranged from ~0.2 nm to ~0.9 nm with an average of 0.55 nm and a standard error of 0.02 nm. Nanoparticle edges in the middle panel are highlighted by blue dotted lines.

Following its formation, a neck grows laterally across the interface between nanoparticles producing a grain boundary. The structures of these grain boundaries are expected to impact the properties of the nanoparticle formed by coalescence[67–72] and are therefore worthy of study. We observed a variety of grain boundary structures (Figure 5). Out of 75 instances, twin boundaries

(example in Figure 5a) were observed in at least 14 instances, and single-crystal structures (example in Figure 5b), for which lattice fringes were equivalent on either side of the boundary, were observed in 2 instances. Other structures were also observed. There were 11 crystalline grain boundaries (example shown in Figure 5c) for which lattice fringes on either side of the grain boundary intersect at the boundary with an angle, $\Delta\theta < 15$ °. There were 24 amorphous or partially crystalline grain boundaries (example in Figure 5d) for which lattice fringes on either side of the boundary cross at an angle $\Delta\theta > 15°$. In 26 of 75 instances, there was insufficient lattice information for assigning crystallinity. Details of the analysis are provided in SI. In several cases, the structures of grain boundaries were not static: grain growth[73] was observed wherein polycrystalline nanostructures formed right after coalescence evolved into single crystalline final structure (Figure S5).

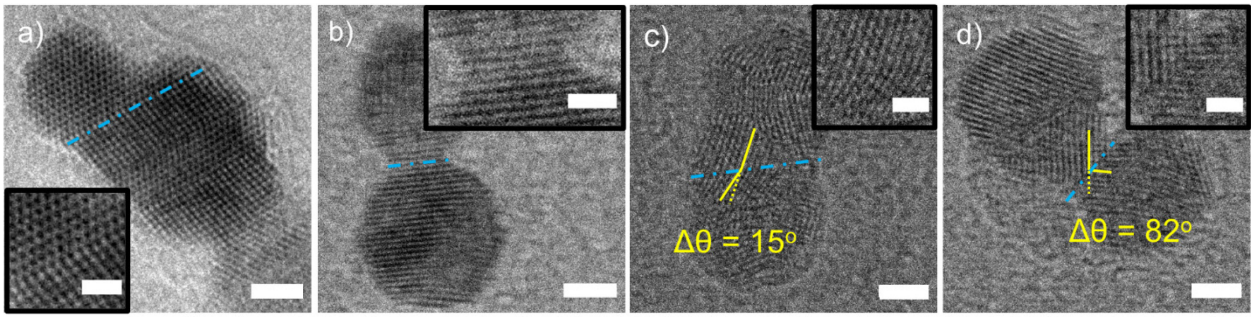

Figure 5. Grain boundaries formed in the course of electron-beam-induced coalescence. Examples of different types of grain boundaries: (a) twin boundary, (b) a single-crystal structure, (c) crystalline grain boundary with $\Delta\theta = 15°$, and (d) amorphous or partially crystalline grain boundary with $\Delta\theta = 82°$. Scale bars are 2 nm in length. Blue dashed lines indicate where the boundary is in each structure. Insets are magnified views in the grain boundary region and have scale bars of 1 nm length.

While these results introduce an interesting photoinduced phenomenon, there are many open questions and avenues to pursue in the future. For instance, which carriers, are involved in the process: excited sp-band electrons, sp-band holes, and/or d-band holes? This question could be answered by studying the Ostwald ripening kinetics as a function of the excitation wavelength from the red tail of the LSPR (where both intraband sp → sp transitions dominate) across the LSPR peak (where both intraband sp → sp and interband d → sp transitions are excited) to the blue region of the spectrum (where the highest-energy interband d → sp transitions are excited). Such a study will also reveal if LSPR excitations are indispensable for inducing the dynamics observed here. On another front, is the observed phenomenon specific to Au–Cu alloy nanoparticles? Perhaps, the high diffusivity of Cu is a critical factor. We can test this hypothesis by studying similarly sized monometallic Au nanoparticles and Cu nanoparticles as well as nanoparticles of

other plasmonic metals. Finally, we can verify the proposed involvement of surface phonon excitations by studying the kinetics of plasmon-induced Ostwald ripening as a function of the nanoparticle size: in smaller nanoparticles, due to the higher surface-to-volume ratios, electron–surface phonon scattering is more efficient as it can effectively compete with electron–bulk phonon scattering.[63]

Conclusions:

Using a DETEM equipped with the capability of laser excitation of the specimen, we monitored in real time with nanoscale spatial resolution a host of structural processes induced in Au–Cu alloy nanoparticles under plasmonic excitation. Plasmon excitation was found to induce the Ostwald ripening of closely spaced nanoparticles in a switch-like kinetic manner. These results inform us about potential transformations of plasmonic nanostructures that can occur under operating conditions of plasmonic photocatalysis or plasmon-assisted electrocatalysis where a high areal density of plasmonic nanoparticles supported on a substrate is subjected to continuous light excitation. The sizes, shapes, and defect profiles of the nanostructures formed by plasmon-induced Ostwald ripening will impact their catalytic properties under operating conditions.[18,20]

Supporting Information:

The Supporting Information is available free of charge at https://pubs.acs.org/doi/10.1021/acs.jpcc.3c04035.

Further details of synthesis, characterization, in situ 308 TEM experiments, and data analysis; additional example of plasmon-induced Ostwald ripening; results from control study of the effect of elevated temperatures in the absence of plasmonic excitation; information about outcome morphologies in electron-beam-induced coalescence and single-crystalline nanostructures formed by healing of grain boundaries; and captions for supporting movie (PDF) Supporting Movie 1 of a nanoparticle undergoing Ostwald ripening under plasmonic excitation (AVI)

Acknowledgements:

This material is based on work supported by the National Science Foundation under Grant CHE-2304910. Funding for this work was provided in part (support for F.M.A) by the Robert C. and Carolyn J. Springborn Endowment and the Future Interdisciplinary Research Explorations (FIRE)

grant from the UIUC College of Agricultural, Consumer, and Environmental Sciences. M.C. was supported by the Clare Boothe Luce Program. P.K.J. is thankful for the support of the John Simon Memorial Guggenheim Foundation in the form of a Guggenheim Fellowship. R.M.v.d.V. acknowledges support from the David and Lucile Packard Foundation, as well as John and Margaret Witt (private funds). The work was carried out in part at the Materials Research Laboratory Central Research Facilities, University of Illinois. We acknowledge Dr. Jim Mabon and Dr. Changqiang Chen for maintenance of the DETEM and Chang Qian for providing calibration data for the US1000 camera used in this work.

Author Contributions

F.M.A. prepared and characterized materials, designed and conducted experiments, performed analyses, and cowrote the manuscript. M.C. prepared and characterized materials and cowrote manuscript. R.M.v.d.V. provided analyses and cowrote manuscript. P. K. J. conceived project, designed studies, provided analyses and models, and cowrote manuscript.

References:

(1) Brongersma, M. L.; Halas, N. J.; Nordlander, P. Plasmon-Induced Hot Carrier Science and Technology. *Nat. Nanotechnol.* **2015**, *10*, 25–34. https://doi.org/10.1038/nnano.2014.311.

(2) Wang, L.; Hasanzadeh Kafshgari, M.; Meunier, M. Optical Properties and Applications of Plasmonic-Metal Nanoparticles. *Adv. Funct. Mater.* **2020**, *30*, 2005400. https://doi.org/10.1002/adfm.202005400.

(3) Linic, S.; Aslam, U.; Boerigter, C.; Morabito, M. Photochemical Transformations on Plasmonic Metal Nanoparticles. *Nat. Mater.* **2015**, *14*, 567–576. https://doi.org/10.1038/nmat4281.

(4) Yu, S.; Wilson, A. J.; Heo, J.; Jain, P. K. Plasmonic Control of Multi-Electron Transfer and C-C Coupling in Visible-Light-Driven CO_2 Reduction on Au Nanoparticles. *Nano Lett.* **2018**, *18*, 2189–2194. https://doi.org/10.1021/acs.nanolett.7b05410.

(5) Swearer, D. F.; Zhao, H.; Zhou, L.; Zhang, C.; Robatjazi, H.; Martirez, J. M. P.; Krauter, C. M.; Yazdi, S.; McClain, M. J.; Ringe, E.; et al. Heterometallic Antenna-Reactor Complexes for Photocatalysis. *Proc. Natl. Acad. Sci. U. S. A.* **2016**, *113*, 8916–8920. https://doi.org/10.1073/pnas.1609769113.

(6) Yang, J.; Guo, Y.; Lu, W.; Jiang, R.; Wang, J. Emerging Applications of Plasmons in Driving CO_2 Reduction and N_2 Fixation. *Adv. Mater.* **2018**, *30*, 1802227. https://doi.org/10.1002/adma.201802227.

(7) Kneipp, J.; Kneipp, H.; Kneipp, K. SERS—a Single-Molecule and Nanoscale Tool for Bioanalytics. *Chem. Soc. Rev.* **2008**, *37*, 1052–1060. https://doi.org/10.1039/b708459p.

(8) Kneipp, K.; Wang, Y.; Kneipp, H.; Perelman, L. T.; Itzkan, I.; Dasari, R. R.; Feld, M. S. Single Molecule Detection Using Surface-Enhanced Raman Scattering (SERS). *Phys. Rev. B - Condens. Matter Mater. Phys.* **1997**, *78*, 1667–1670. https://doi.org/10.1103/PhysRevLett.78.1667.

(9) Devasia, D.; Wilson, A. J.; Heo, J.; Mohan, V.; Jain, P. K. A Rich Catalog of C–C Bonded Species Formed in CO_2 Reduction on a Plasmonic Photocatalyst. *Nat. Commun.* **2021**, *12*, 2612. https://doi.org/10.1038/s41467-021-22868-9.

(10) Gurav, D. D.; Jia, Y.; Ye, J.; Qian, K. Design of Plasmonic Nanomaterials for Diagnostic Spectrometry. *Nanoscale Adv.* **2019**, *1*, 459–469. https://doi.org/10.1039/c8na00319j.

(11) Ayala-Orozco, C.; Urban, C.; Knight, M. W.; Urban, A. S.; Neumann, O.; Bishnoi, S. W.; Mukherjee, S.; Goodman, A. M.; Charron, H.; Mitchell, T.; et al. Au Nanomatryoshkas as Efficient Near-Infrared Photothermal Transducers for Cancer Treatment: Benchmarking against Nanoshells. *ACS Nano* **2014**, *8*, 6372–6381. https://doi.org/10.1021/nn501871d.

(12) Clavero, C. Plasmon-Induced Hot-Electron Generation at Nanoparticle/Metal-Oxide Interfaces for Photovoltaic and Photocatalytic Devices. *Nat. Photonics* **2014**, *8*, 95–103. https://doi.org/10.1038/nphoton.2013.238.

(13) Oulton, R. F.; Sorger, V. J.; Zentgraf, T.; Ma, R. M.; Gladden, C.; Dai, L.; Bartal, G.; Zhang, X. Plasmon Lasers at Deep Subwavelength Scale. *Nature* **2009**, *461*, 629–632. https://doi.org/10.1038/nature08364.

(14) Ma, R. M.; Oulton, R. F.; Sorger, V. J.; Zhang, X. Plasmon Lasers: Coherent Light Source at Molecular Scales. *Laser Photonics Rev.* **2013**, *7*, 1–21. https://doi.org/10.1002/lpor.201100040.

(15) Manjavacas, A.; Liu, J. G.; Kulkarni, V.; Nordlander, P. Plasmon-Induced Hot Carriers in Metallic Nanoparticles. *ACS Nano* **2014**, *8*, 7630–7638. https://doi.org/10.1021/nn502445f.

(16) Sherry, L. J.; Chang, S.-H.; Schatz, G. C.; Van Duyne, R. P. Localized Surface Plasmon Resonance of Single Silver Nanocubes. *Nano Lett.* **2005**, *5*, 2034–2038. https://doi.org/10.4028/www.scientific.net/AMR.818.137.

(17) Jain, P. K.; Lee, K. S.; El-Sayed, I. H.; El-Sayed, M. A. Calculated Absorption and Scattering Properties of Gold Nanoparticles of Different Size, Shape, and Composition: Applications in Biological Imaging and Biomedicine. *J. Phys. Chem. B* **2006**, *110*, 7238–7248. https://doi.org/10.1021/jp057170o.

(18) Wang, Y.; Liu, J.; Wang, Y.; Al-Enizi, A. M.; Zheng, G. Tuning of CO_2 Reduction Selectivity on Metal Electrocatalysts. *Small* **2017**, *13*, 1701809. https://doi.org/10.1002/smll.201701809.

(19) Chou, T. C.; Chang, C. C.; Yu, H. L.; Yu, W. Y.; Dong, C. L.; Velasco-Vélez, J. J.; Chuang,

C. H.; Chen, L. C.; Lee, J. F.; Chen, J. M.; et al. Controlling the Oxidation State of the Cu Electrode and Reaction Intermediates for Electrochemical CO_2 Reduction to Ethylene. *J. Am. Chem. Soc.* **2020**, *142*, 2857–2867. https://doi.org/10.1021/jacs.9b11126.

(20) Zhou, X.; Xu, W.; Liu, G.; Panda, D.; Chen, P. Size-Dependent Catalytic Activity and Dynamics of Gold Nanoparticles at the Single-Molecule Level. *J. Am. Chem. Soc.* **2010**, *132*, 138–146. https://doi.org/10.1021/ja904307n.

(21) He, Y.; Liu, J. C.; Luo, L.; Wang, Y. G.; Zhu, J.; Du, Y.; Li, J.; Mao, S. X.; Wang, C. Size-Dependent Dynamic Structures of Supported Gold Nanoparticles in CO Oxidation Reaction Condition. *Proc. Natl. Acad. Sci. U. S. A.* **2018**, *115*, 7700–7705. https://doi.org/10.1073/pnas.1800262115.

(22) Routzahn, A. L.; Jain, P. K. Single-Nanocrystal Reaction Trajectories Reveal Sharp Cooperative Transitions. *Nano Lett.* **2014**, *14*, 987–992. https://doi.org/10.1021/nl4044289.

(23) Smith, J. G.; Yang, Q.; Jain, P. K. Identification of a Critical Intermediate in Galvanic Exchange Reactions by Single-Nanoparticle-Resolved Kinetics. *Angew. Chem. Int. Ed.* **2014**, *53*, 2867–2872. https://doi.org/10.1002/anie.201309307.

(24) Susman, M. D.; Feldman, Y.; Bendikov, T. A.; Vaskevich, A.; Rubinstein, I. Real-Time Plasmon Spectroscopy Study of the Solid-State Oxidation and Kirkendall Void Formation in Copper Nanoparticles. *Nanoscale* **2017**, *9*, 12573–12589. https://doi.org/10.1039/c7nr04256f.

(25) Smith, J. G.; Chakraborty, I.; Jain, P. K. In Situ Single-Nanoparticle Spectroscopy Study of Bimetallic Nanostructure Formation. *Angew. Chem. Int. Ed.* **2016**, *55*, 9979–9983. https://doi.org/10.1002/anie.201604710.

(26) Routzahn, A. L.; Jain, P. K. Luminescence Blinking of a Reacting Quantum Dot. *Nano Lett.* **2015**, *15*, 2504–2509. https://doi.org/10.1021/acs.nanolett.5b00068.

(27) Tao, F.; Grass, M. E.; Zhang, Y.; Butcher, D. R.; Renzas, J. R.; Liu, Z.; Chung, J. Y.; Mun, B. S.; Salmeron, M.; Somorjai, G. A. Reaction-Driven Restructuring of Rh-Pd and Pt-Pd Core-Shell Nanoparticles. *Science* **2008**, *322*, 932–934. https://doi.org/10.1126/science.1164170.

(28) Tao, F.; Grass, M. E.; Zhang, Y.; Butcher, D. R.; Aksoy, F.; Aloni, S.; Altoe, V.; Alayoglu, S.; Renzas, J. R.; Tsung, C. K.; et al. Evolution of Structure and Chemistry of Bimetallic Nanoparticle Catalysts under Reaction Conditions. *J. Am. Chem. Soc.* **2010**, *132*, 8697–8703. https://doi.org/10.1021/ja101502t.

(29) Gibson, E. K.; Beale, A. M.; Catlow, C. R. A.; Chutia, A.; Gianolio, D.; Gould, A.; Kroner, A.; Mohammed, K. M. H.; Perdjon, M.; Rogers, S. M.; et al. Restructuring of AuPd Nanoparticles Studied by a Combined XAFS/DRIFTS Approach. *Chem. Mater.* **2015**, *27*, 3714–3720. https://doi.org/10.1021/acs.chemmater.5b00866.

(30) Kashin, A. S.; Ananikov, V. P. Monitoring Chemical Reactions in Liquid Media Using Electron Microscopy. *Nat. Rev. Chem.* **2019**, *3*, 624–637. https://doi.org/10.1038/s41570-019-0133-z.

(31) Xin, H. L.; Alayoglu, S.; Tao, R.; Genc, A.; Wang, C. M.; Kovarik, L.; Stach, E. A.; Wang, L. W.; Salmeron, M.; Somorjai, G. A.; et al. Revealing the Atomic Restructuring of Pt-Co Nanoparticles. *Nano Lett.* **2014**, *14*, 3203–3207. https://doi.org/10.1021/nl500553a.

(32) Vendelbo, S. B.; Elkjær, C. F.; Falsig, H.; Puspitasari, I.; Dona, P.; Mele, L.; Morana, B.; Nelissen, B. J.; van Rijn, R.; Creemer, J. F.; et al. Visualization of Oscillatory Behaviour of Pt Nanoparticles Catalysing CO Oxidation. *Nat. Mater.* **2014**, *13*, 884–890. https://doi.org/10.1038/nmat4033.

(33) Chee, S. W.; Tan, S. F.; Baraissov, Z.; Bosman, M.; Mirsaidov, U. Direct Observation of the Nanoscale Kirkendall Effect during Galvanic Replacement Reactions. *Nat. Commun.* **2017**, *8*, 1224. https://doi.org/10.1038/s41467-017-01175-2.

(34) Heo, J.; Torres, D. D.; Banerjee, P.; Jain, P. K. In-Situ Electron Microscopy Mapping of an Order-Disorder Transition in a Superionic Conductor. *Nat. Commun.* **2019**, *10*, 1505. https://doi.org/10.1038/s41467-019-09502-5.

(35) Heo, J.; Cho, K. H.; Jain, P. K. Motion of Defects in Ion-Conducting Nanowires. *Nano Lett.* **2021**, *21*, 556–561. https://doi.org/10.1021/acs.nanolett.0c04056.

(36) Alcorn, F. M.; Jain, P. K.; van der Veen, R. M. Time-Resolved Transmission Electron Microscopy for Nanoscale Chemical Dynamics. *Nat. Rev. Chem.* **2023**, *7*, 256–272.

https://doi.org/10.1038/s41570-023-00469-y.

(37) Yang, J.; Zeng, Z.; Kang, J.; Betzler, S.; Czarnik, C.; Zhang, X.; Ophus, C.; Yu, C.; Bustillo, K.; Pan, M.; et al. Formation of Two-Dimensional Transition Metal Oxide Nanosheets with Nanoparticles as Intermediates. *Nat. Mater.* **2019**, *18*, 970–976. https://doi.org/10.1038/s41563-019-0415-3.

(38) Sohn, S.; Xie, Y.; Jung, Y.; Schroers, J.; Cha, J. J. Tailoring Crystallization Phases in Metallic Glass Nanorods via Nucleus Starvation. *Nat. Commun.* **2017**, *8*, 1980. https://doi.org/10.1038/s41467-017-02153-4.

(39) Taheri, M. L.; Stach, E. A.; Arslan, I.; Crozier, P. A.; Kabius, B. C.; LaGrange, T.; Minor, A. M.; Takeda, S.; Tanase, M.; Wagner, J. B.; et al. Current Status and Future Directions for in Situ Transmission Electron Microscopy. *Ultramicroscopy* **2016**, *170*, 86–95. https://doi.org/10.1016/j.ultramic.2016.08.007.

(40) van der Veen, R. M.; Kwon, O. H.; Tissot, A.; Hauser, A.; Zewail, A. H. Single-Nanoparticle Phase Transitions Visualized by Four-Dimensional Electron Microscopy. *Nat. Chem.* **2013**, *5*, 395–402. https://doi.org/10.1038/nchem.1622.

(41) Żak, A. M. Light-Induced in Situ Transmission Electron Microscopy-Development, Challenges, and Perspectives. *Nano Lett.* **2022**, *22*, 9219–9226. https://doi.org/10.1021/acs.nanolett.2c03669.

(42) Sytwu, K.; Vadai, M.; Hayee, F.; Angell, D. K.; Dai, A.; Dixon, J.; Dionne, J. A. Driving Energetically Unfavorable Dehydrogenation Dynamics with Plasmonics. *Science* **2021**, *371*, 280–283. https://doi.org/10.1126/science.abd2847.

(43) Vadai, M.; Angell, D. K.; Hayee, F.; Sytwu, K.; Dionne, J. A. In-Situ Observation of Plasmon-Controlled Photocatalytic Dehydrogenation of Individual Palladium Nanoparticles. *Nat. Commun.* **2018**, *9*, 4658. https://doi.org/10.1038/s41467-018-07108-x.

(44) Zhang, L.; Miller, B. K.; Crozier, P. A. Atomic Level in Situ Observation of Surface Amorphization in Anatase Nanocrystals during Light Irradiation in Water Vapor. *Nano Lett.* **2013**, *13*, 679–684. https://doi.org/10.1021/nl304333h.

(45) LaGrange, T.; Armstrong, M. R.; Boyden, K.; Brown, C. G.; Campbell, G. H.; Colvin, J.

D.; DeHope, W. J.; Frank, A. M.; Gibson, D. J.; Hartemann, F. V.; et al. Single-Shot Dynamic Transmission Electron Microscopy. *Appl. Phys. Lett.* **2006**, *89*, 044105. https://doi.org/10.1063/1.2236263.

(46) Adhikari, A.; Eliason, J. K.; Sun, J.; Bose, R.; Flannigan, D. J.; Mohammed, O. F. Four-Dimensional Ultrafast Electron Microscopy: Insights into an Emerging Technique. *ACS Appl. Mater. Interfaces* **2017**, *9*, 3–16. https://doi.org/10.1021/acsami.6b12301.

(47) Campbell, G. H.; McKeown, J. T.; Santala, M. K. Time Resolved Electron Microscopy for in Situ Experiments. *Appl. Phys. Rev.* **2014**, *1*, 041101. https://doi.org/10.1063/1.4900509.

(48) Vanacore, G. M.; Fitzpatrick, A. W. P.; Zewail, A. H. Four-Dimensional Electron Microscopy: Ultrafast Imaging, Diffraction and Spectroscopy in Materials Science and Biology. *Nano Today* **2016**, *11*, 228–249. https://doi.org/10.1016/j.nantod.2016.04.009.

(49) Barwick, B.; Flannigan, D. J.; Zewail, A. H. Photon-Induced Near-Field Electron Microscopy. *Nature* **2009**, *462*, 902–906. https://doi.org/10.1038/nature08662.

(50) McKenna, A. J.; Eliason, J. K.; Flannigan, D. J. Spatiotemporal Evolution of Coherent Elastic Strain Waves in a Single MoS_2 Flake. *Nano Lett.* **2017**, *17*, 3952–3958. https://doi.org/10.1021/acs.nanolett.7b01565.

(51) Kim, Y. J.; Jung, H.; Han, S. W.; Kwon, O. H. Ultrafast Electron Microscopy Visualizes Acoustic Vibrations of Plasmonic Nanorods at the Interfaces. *Matter* **2019**, *1*, 481–495. https://doi.org/10.1016/j.matt.2019.03.004.

(52) Danz, T.; Domrose, T.; Ropers, C. Ultrafast Nanoimaging of the Order Parameter in a Structural Phase Transition. *Science* **2021**, *374*, 371–374. https://doi.org/10.1126/science.abd2774.

(53) Zandi, O.; Sykes, A. E.; Cornelius, R. D.; Alcorn, F. M.; Zerbe, B. S.; Duxbury, P. M.; Reed, B. W.; van der Veen, R. M. Transient Lensing from a Photoemitted Electron Gas Imaged by Ultrafast Electron Microscopy. *Nat. Commun.* **2020**, *11*, 3001. https://doi.org/10.1038/s41467-020-16746-z.

(54) Kim, D.; Resasco, J.; Yu, Y.; Asiri, A. M.; Yang, P. Synergistic Geometric and Electronic Effects for Electrochemical Reduction of Carbon Dioxide Using Gold-Copper Bimetallic

Nanoparticles. *Nat. Commun.* **2014**, *5*, 4948. https://doi.org/10.1038/ncomms5948.

(55) Neatu, ţtefan; Maciá-Agullò, J. A.; Concepciòn, P.; Garcia, H. Gold-Copper Nanoalloys Supported on TiO_2 as Photocatalysts for CO_2 Reduction by Water. *J. Am. Chem. Soc.* **2014**, *136*, 15969–15976. https://doi.org/10.1021/ja506433k.

(56) Peng, S.; Lee, Y.; Wang, C.; Yin, H.; Dai, S.; Sun, S. A Facile Synthesis of Monodisperse Au Nanoparticles and Their Catalysis of CO Oxidation. *Nano Res.* **2008**, *1*, 229–234. https://doi.org/10.1007/s12274-008-8026-3.

(57) Chen, W.; Yu, R.; Li, L.; Wang, A.; Peng, Q.; Li, Y. A Seed-Based Diffusion Route to Monodisperse Intermetallic CuAu Nanocrystals. *Angew. Chem. Int. Ed.* **2010**, *49*, 2917–2921. https://doi.org/10.1002/anie.200906835.

(58) Salmon, A. R.; Kleemann, M. E.; Huang, J.; Deacon, W. M.; Carnegie, C.; Kamp, M.; de Nijs, B.; Demetriadou, A.; Baumberg, J. J. Light-Induced Coalescence of Plasmonic Dimers and Clusters. *ACS Nano* **2020**, *14*, 4982–4987. https://doi.org/10.1021/acsnano.0c01213.

(59) Weng, B.; Jiang, Y.; Liao, H. G.; Roeffaers, M. B. J.; Lai, F.; Huang, H.; Tang, Z. Visualizing Light-Induced Dynamic Structural Transformations of Au Clusters-Based Photocatalyst via in Situ TEM. *Nano Res.* **2021**, *14*, 2805–2809. https://doi.org/10.1007/s12274-021-3289-z.

(60) Taylor, P. Ostwald Ripening in Emulsions. *Adv. Colloid Interface Sci.* **1998**, *75*, 107–163. https://doi.org/10.1016/S0001-8686(98)00035-9.

(61) Kabalnov, A. Ostwald Ripening and Related Phenomena. *J. Dispers. Sci. Technol.* **2001**, *22*, 1–12. https://doi.org/10.1081/DIS-100102675.

(62) Smith, J. G.; Yang, Q.; Jain, P. K. Identification of a Critical Intermediate in Galvanic Exchange Reactions by Single-Nanoparticle-Resolved Kinetics. *Angew. Chem.* **2014**, *126*, 2911–2916. https://doi.org/10.1002/ange.201309307.

(63) Jain, P. K.; Qian, W.; El-Sayed, M. A. Ultrafast Cooling of Photoexcited Electrons in Gold Nanoparticle-Thiolated DNA Conjugates Involves the Dissociation of the Gold-Thiol Bond. *J. Am. Chem. Soc.* **2006**, *128*, 2426–2433. https://doi.org/10.1021/ja056769z.

(64) Tom, H. W. K.; Aumiller, G. D.; Brito-Cruz, C. H. Time-Resolved Study of Laser-Induced Disorder of Si Surfaces. *Phys. Rev. Lett.* **1988**, *60*, 1438–1441. https://doi.org/10.1103/PhysRevLett.60.1438.

(65) Shank, C. V.; Yen, R.; Hirlimann, C. Femtosecond-Time-Resolved Surface Structural Dynamics of Optically Excited Silicon. *Phys. Rev. Lett.* **1983**, *51*, 900–902. https://doi.org/10.1103/PhysRevLett.51.900.

(66) Zhang, Y.; Flannigan, D. J. Imaging Nanometer Phonon Softening at Crystal Surface Steps with 4D Ultrafast Electron Microscopy. *Nano Lett.* **2021**, *21*, 7332–7338. https://doi.org/10.1021/acs.nanolett.1c02524.

(67) Weng, W.-L.; Chen, H.-Y.; Ting, Y.-H.; Chen, H.-Y. T.; Wu, W.-W.; Tu, K.-N.; Liao, C.-N. Twin-Boundary Reduced Surface Diffusion on Electrically Stressed Copper Nanowires. *Nano Lett.* **2022**, *22*, 9071–9076. https://doi.org/10.1021/acs.nanolett.2c03437.

(68) Wang, X.; Zheng, S.; Deng, C.; Weinberger, C. R.; Wang, G.; Mao, S. X. In Situ Atomic-Scale Observation of 5-Fold Twin Formation in Nanoscale Crystal under Mechanical Loading. *Nano Lett.* **2023**, *23*, 514–522. https://doi.org/10.1021/acs.nanolett.2c03852.

(69) Zhu, Q.; Huang, Q.; Guang, C.; An, X.; Mao, S. X.; Yang, W.; Zhang, Z.; Gao, H.; Zhou, H.; Wang, J. Metallic Nanocrystals with Low Angle Grain Boundary for Controllable Plastic Reversibility. *Nat. Commun.* **2020**, *11*, 3100. https://doi.org/10.1038/s41467-020-16869-3.

(70) Feng, X.; Jiang, K.; Fan, S.; Kanan, M. W. Grain-Boundary-Dependent CO_2 Electroreduction Activity. *J. Am. Chem. Soc.* **2015**, *137*, 4606–4609. https://doi.org/10.1021/ja5130513.

(71) Chen, Z.; Wang, T.; Liu, B.; Cheng, D.; Hu, C.; Zhang, G.; Zhu, W.; Wang, H.; Zhao, Z. J.; Gong, J. Grain-Boundary-Rich Copper for Efficient Solar-Driven Electrochemical CO2 Reduction to Ethylene and Ethanol. *J. Am. Chem. Soc.* **2020**, *142*, 6878–6883. https://doi.org/10.1021/jacs.0c00971.

(72) Song, M.; Zhou, G.; Lu, N.; Lee, J.; Nakouzi, E.; Wang, H.; Li, D. Oriented Attachment Induces Fivefold Twins by Forming and Decomposing High-Energy Grain Boundaries.

Science **2020**, *367*, 40–45. https://doi.org/10.1017/cbo9781316389508.016.

(73) Ingham, B.; Lim, T. H.; Dotzler, C. J.; Henning, A.; Toney, M. F.; Tilley, R. D. How Nanoparticles Coalesce: An in Situ Study of Au Nanoparticle Aggregation and Grain Growth. *Chem. Mater.* **2011**, *23*, 3312–3317. https://doi.org/10.1021/cm200354d.